Ion-matter interaction: the three-dimensional version of the thermal spike model. Application to nanoparticle irradiation with swift heavy ions

Ion-matter interaction: the three-dimensional version of the thermal spike model. Application to nanoparticle irradiation with swift heavy ions

Ch Dufour[1], V Khomenkov[1], G Rizza[2] and M Toulemonde[1]

[1] CIMAP, CEA / CNRS / ENSICAEN / Université de Caen, 6 Boulevard du Maréchal Juin, 14050 Caen cedex 4, France
[2] Ecole Polytechnique, Laboratoire des Solides Irradiés (LSI) CEA/DSM/IRAMIS, CNRS 91128 Palaiseau Cedex, France

E-mail: christian.dufour@ensicaen.fr

Abstract
In the framework of swift heavy ion–matter interaction, the thermal spike has proved its worth for nearly two decades. This paper deals with the necessary refinement of the computation due to the kind of materials of interest, i.e. nanomaterials such as multilayered systems or composite films constituted of nanocylinders or nanospheres embedded in an insulating matrix. The three-dimensional computation of the thermal spike model is applied for the first time in the case of ions striking layers containing spherical nanoparticles embedded in a silica matrix. The temperature profiles calculated at each point (x, y, z) of the target for a total duration up to 10^{-10} s and different values of ion impact parameter allow a possible explanation of the particle shape change under irradiation with swift heavy ions having an energy of several MeV amu^{-1}

(Some figures may appear in colour only in the online journal)

1. Metallic nanoparticles synthesis with ion beam size and shape

Over a decade, materials based on nanoparticles embedded in a dielectric matrix have been elaborated with various techniques, among which is the use of swift heavy ion irradiations [1]. Such kinds of materials have been found interesting because of their peculiar optical properties related to plasmon excitation by UV–visible radiation [2]. Potential applications are expected, particularly in the field of optical sensors. It has been demonstrated that plasmon frequency depends on the particle size, on the shape (spherical, cylindrical) and also on the surrounding matrix [3, 4]. It is then important to monitor such geometrical parameters with the ion beam assisted method cited above. Authors use one-step [3, 5–7] or two-step processes [1, 8] which combine a prior ion implantation with the desired metallic species with a post elaboration irradiation. Since 2003 [1], several papers have invoked the thermal spike process leading to the shaping of nanoparticles [9–11] and we particularly refer to the work of

Ridgway *et al* [12]. We have been among the first teams to develop a numerical solution of this model since 1992 [13]. A wide range of materials have been successfully described: metals [14–16], semiconducting and insulators [17, 18]. In this paper, we propose the first real 3D version of the model which proves necessary in cases where the usual cylindrical symmetry is no longer valid: anisotropic thermal parameters and/or anisotropy in the geometry of the physical problem. We first discuss the thermal parameters that need special attention in order to give quantitative information instead of qualitative description. This discussion is made in relation to the work of Awazu *et al* [19] and gives light on the choice of the thermal parameters. We therefore perform our simulation for the materials and ions studied in [19]: cylindrical gold nanoparticles embedded in silica and irradiated with Br 110 MeV. Then we focus on the application of the model to the nanoparticle transformation under irradiation with swift heavy ions and show the difference between cylindrical and spherical particles such as those investigated in [9–12]. Finally

Table 1. Physical parameters of SiO$_2$ and Au.

Material	SiO$_2$	Au
ρ_S (g cm^{-3})	2.32	19.3
ρ_L (g cm^{-3})	2.32	17.3
T_m (K)	1972	1337
T_v (K)	3223	3130
Q_m (J/g)	142	63.7
Q_v (J/g)	4715	1645
g (W cm^{-3} K^{-1})	1.25×10^{13} [19]	2.3×10^{10} [15]
S_e (keV nm^{-1})	9.7	29.2
S_n (keV nm^{-1})	0.025	0.113

Figure 1. Geometry of the calculation box.

we describe the thermal behaviour of a spherical particle due to an ion impact.

2. The 3D thermal spike model

The target material is considered as a two-component system: the atomic lattice and the electrons characterized by their respective temperatures T_a and T_e. Starting from the set of coupled equations (1*a*) and (1*b*) governing the electronic and atomic temperatures (T_e and T_a), every physical parameter may now depends on the position $\vec{r}(x, y, z)$ in space. We write the energy variation $dQ = C\,dT$ linked to the temperature variation dT of an elementary volume dV characterized by a specific heat C. dQ is due to three terms: (i) the energy brought by the incident ion on the electrons ($A_e(\vec{r}, t)$) and on the atomic lattice ($A_a(\vec{r}, t)$), (ii) Fick's thermal diffusion law which defines the heat flux $\vec{j} = \overline{\overline{K}} \cdot \nabla T$ where the thermal conductivity $\overline{\overline{K}}$ is a 3×3 matrix and (iii) the energy exchange between electrons and atomic lattice proportional to the temperature difference $g(\vec{r}, t)(T_e - T_a)$ where $g(\vec{r}, t)$ the electron phonon coupling constant.

$$C_e \frac{\partial T_e}{\partial t} = \nabla(K_e \cdot \nabla T_e) - g(T_e - T_a) + A_e \quad (1a)$$

$$C_a \frac{\partial T_a}{\partial t} = \nabla(\overline{\overline{K_a}} \cdot \nabla T_a) + g(T_e - T_a) + A_a. \quad (1b)$$

We describe the different terms in the following sections.

2.1. Incident ion energy deposition

The linear energy transfer from the incident ion to the target atoms (S_n) and electrons (S_e) was computed using the SRIM code by Biersack *et al* [20] and shown in table 1. In the case of swift ions $S_n/S_e < 10^{-2}$ so that we neglect the nuclear component A_a and deal only with electronic one A_e.

We suppose that the incident ion hits the target parallel to the z-axis on (x_0, y_0) point in the XY-plane (figure 1). We separate the space and time variables so that $A_e(\vec{r}, t) = F(\vec{r})G(t)$. The function $G(t)$ is a time pulse of a few femtoseconds duration ($t_0 = 2 \times 10^{-15}$ s), and is normalized so that $\int_0^{t_0} G(t)\,dt = 1$.

The function $F(\vec{r})$ is a product

$$F(\vec{r}) = C\,S_e(x_0, y_0, z)\,\nu^2(x, y, z)\,W(r_\perp).$$
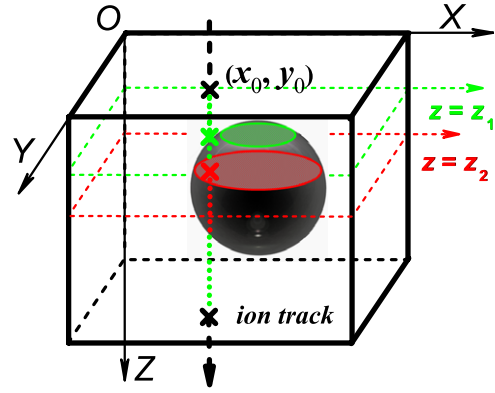
Here we introduce new parameters:

$\nu(x, y, z) = \rho Z/A$ is the parameter proportional to the electron density (ρ is the mass density, Z and A are the atomic and mass numbers of the target material);

$r_\perp(x, y, z) = \bar{\nu}\sqrt{(x - x_0)^2 + (y - y_0)^2}$ is the radial range (in g cm^{-2}) to the ion track, weighted by the mean electron density;

$\bar{\nu} = \int_0^1 \nu[\xi(\vartheta), \eta(\vartheta), z]\,d\vartheta$ where $\xi(\vartheta) = x_0 + (x - x_0)\vartheta$ and $\eta(\vartheta) = y_0 + (y - y_0)\vartheta$.

Finally, $W(r_\perp) = ([1 - (r_\perp + R_{min})/(R_{max} + R_{min})]^{1/\alpha})/(r_\perp (r_\perp + R_{min}))$ is known as the radial δ-ray energy distribution (Waligorski *et al* [21]), where we substitute the range for homogeneous materials with our weighted range $r_\perp$. According to [21], R_{min}, R_{max} are the ranges corresponding to the target ionization potential E_{min} and maximum energy of δ-electrons $E_{max} = 2mc^2\beta^2/(1 - \beta^2)$, β is the incident ion velocity in lightspeed units; $R = k\,E^\alpha$, $k = 6 \times 10^{-6}$ g cm^{-2} keV$^{-\alpha}$; $\alpha = 1.079$ for $\beta < 0.03$ and $\alpha = 1.667$ for $\beta > 0.03$; $W(r_\perp > R_{max}) = 0$.

C is a normalizing constant, so that $\int\int_{-\infty}^\infty F(x, y, z)\,dx\,dy = S_e(z)$.

The energy density transferred to the δ electrons is plotted (in eV atom^{-1}) in the xy-plane for two values of z (figure 2). Hence, we see the distributions in the upper plane ($z = z_1$) for which the ion track is outside the nanoparticle (figure 2(*a*)) and in the bottom plane ($z = z_2$) (figure 2(*b*)). Due to the different electronic densities of the nanoparticle and the matrix, we note that the energy for the same distance from the ion track is higher within the nanoparticle than in the matrix (e.g. see the light blue contour corresponding to a zone in which the energy density exceeds 10 eV atom^{-1}), while the range of energy distribution is shorter. This just reflects the fact that ion energy dissipates with radial distance more efficient in the material with higher electronic density.

2.2. Lattice parameters

The lattice specific heat C_a and thermal conductivity K_a values are a compilation of data from [22–25]. However, for gold, known as a noble metal, the main contribution to measured thermal conductivity comes from the electronic part, especially at low temperature. Hence, in order to estimate the atomic thermal conductivity, we use the relation $K_a = C_a v_S \lambda/3$,
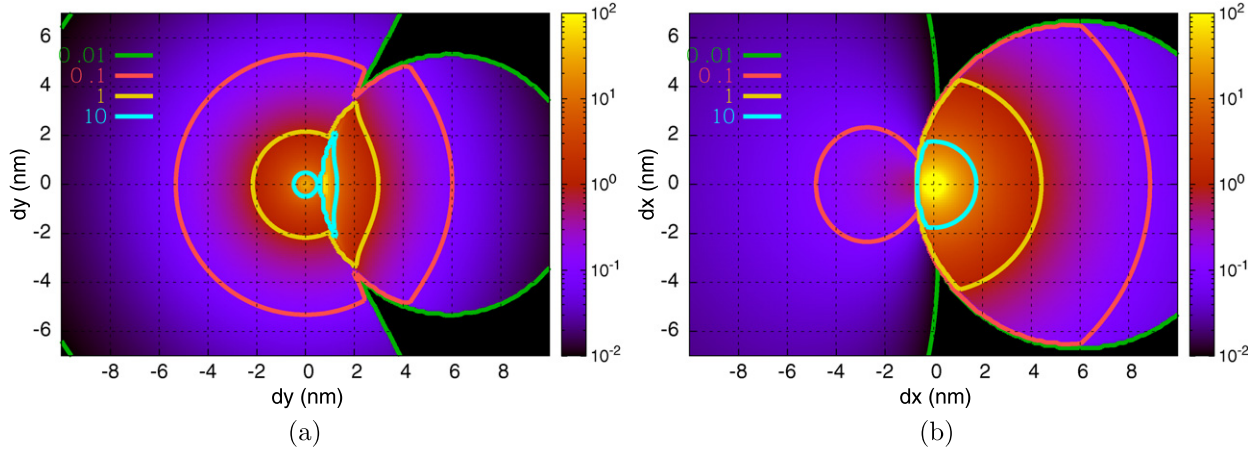
J. Phys. D: Appl. Phys. **45** (2012) 065302

Ch Dufour *et al*

Figure 2. Initial energy distribution on the target electrons (δ-electrons) [eV/atom] in different *XY*-planes for (*a*) $z = z_1$ and (*b*) $z = z_2$.

where v_S is the sound speed and λ is the phonon mean free path (of order of few lattice parameters), in the same way, C_a is taken for classical statistical physics. The temperature dependence of C_a and K_a are plotted in figure 3 and figure 4, respectively (continuous lines: blue for Au and red for SiO$_2$).

The latent heat of phase change, Q_m, is taken into account using the following algorithm described in the case of solid–liquid change that occurs at $T_a = T_m$. For temperatures between $T_m - \Delta T$ and $T_m + \Delta T$, we modify the temperature dependence $C_a(T_a)$ by adding the peak-like function $C_m(T_a)$ to $C_a(T_a)$, so that $\int_{T_m-\Delta T}^{T_m+\Delta T} C_m(T)\, dT = Q_m$, $\Delta T = 5\,\mathrm{K}$ (See the insrt in figure 3). Since the value of C_a becomes high around the melting point, the lattice temperature during melting remains practically constant. A similar modification is done for the vaporizing point.

We mention here that there are a lot of sources referring to the melting temperatures of silica glasses and silica polymorphs, around $1900\,\mathrm{K}\pm500\,\mathrm{K}$. Moreover, we use explicitly here the melting temperature in the middle of this range which corresponds to the value used by Awazu *et al* [19]. Anyway, the most influent parameters on the thermal process in the case of insulating materials are the low thermal conductivity and the high value of electron phonon coupling so that the uncertainty concerning $T_{\mathrm{mSiO_2}}$ does not significantly change the results presented here.

2.3. Electronic parameters

We consider the electronic system in gold as free electron gas. At low temperatures, the electronic specific heat is proportional to the temperature T_e according to [26] ($C_e(T_e) = (\pi^2 k_B n_e/2)(T_e/T_F)$). Here $T_F = ((\hbar^2/2m_e k_B)/(3\pi^2 n_e))^{2/3}$ is the temperature corresponding to the Fermi energy, $\hbar$ and k_B are Planck and Boltzmann constants, m_e and n_e are the electron mass and density, respectively. The high temperature classical value $C_e = \frac{3}{2}k_B n_e$ is valid for $T_e > \frac{3}{\pi^2}T_F$. $C_e(T_e)$ is presented in figure 3 (blue dotted line).

Concerning the thermal conductivity, the relation $K_e = C_e D_e$ is used. The temperature dependence of the electronic diffusivity $D_e(T_e)$ was studied by Martynenko *et al* [27] and
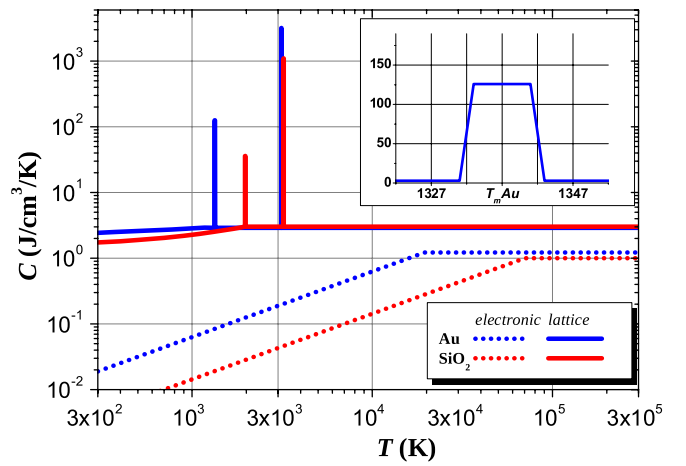

Figure 3. Electronic (C_e in dotted lines) and atomic (C_a in solid lines) specific heats of Au (blue) and SiO$_2$ (red) as a function of temperature
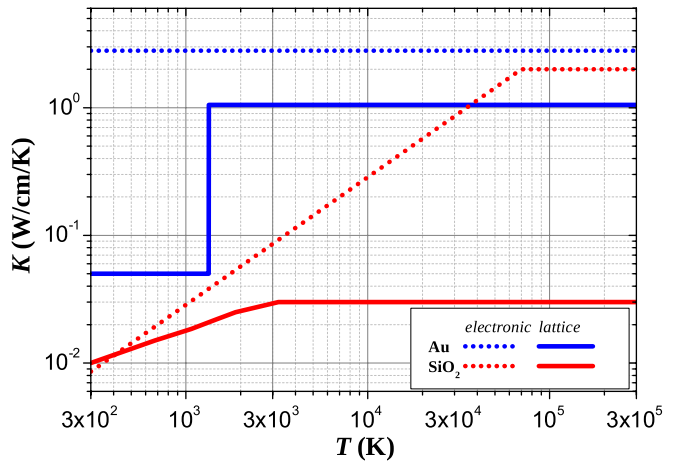

Figure 4. Electronic (K_e in dotted lines) and atomic (K_a in solid lines) thermal conductivities of Au (blue) and SiO$_2$ (red) as a function of temperature.

used here. It was shown that the value of D_e decreases from $\sim10^2\,\mathrm{cm^2\,s^{-1}}$ at 300 K down to $\sim1\,\mathrm{cm^2\,s^{-1}}$ at $T_e \sim 10^4\,\mathrm{K^{-1}}$. Hence, we approximate $D_e(T_e) = 300\frac{D_{300}}{T_e}$ at $T_e < T_{\mathrm{lim}}$, and $D_e = D_{\mathrm{min}}$ at $T_e > T_{\mathrm{lim}}$, with $D_{300} = 150\,\mathrm{cm^2\,s^{-1}}$,
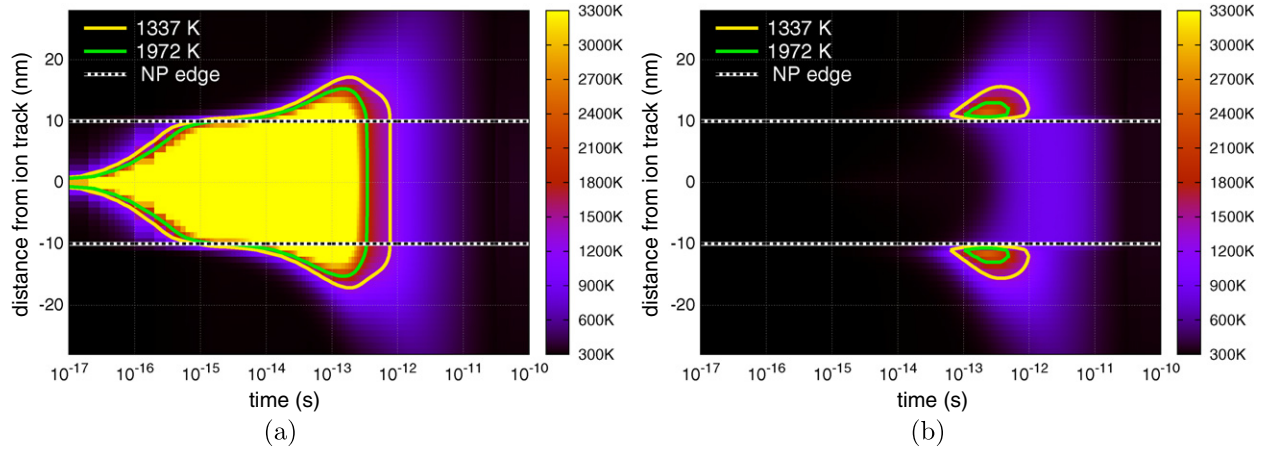
Figure 5. Cylindrical gold nanoparticle (diameter: 20 nm). Evolution of the electronic and atomic temperatures $T_e(r, t)$ and $T_a(r, t)$ in kelvin as a function of radial distance r from the ion path and time t. The thermodynamic parameters are those from Awazu *et al* [19].

$D_{min} = 2 \, \text{cm}^2 \, \text{s}^{-1}$, and $T_{lim} = 300 \frac{D_{300}}{D_{min}}$. Hence the value K_e is plotted versus T_e in figure 4 (blue dotted line).

For the dielectrics, the free electron gas model was adopted for hot electrons [17] with the values of $1 \, \text{J cm}^{-3} \, \text{K}$ for specific heat and of $2 \, \text{W cm}^{-1} \, \text{K}^{-1}$ for thermal conductivity. These values have been considered independent of temperature in the simulations of Awazu *et al* [19]. However, we now consider that such an approach is valid only when the temperature exceeds the bandgap ($E_g = k_B T_g \approx 9 \, \text{eV}$ leading to $T_g \approx 10^5 \, \text{K}$ for SiO_2). At $T_e < T_g$ the fact that only part of atoms are ionized must be taken into account. Here we use linear law for both $C_e(T_e)$ and $K_e(T_e)$ at $T_e < T_g$ (See figures 3 and 4, red dotted lines). This is a way to account for the fact that, in a first-order approximation, the number of electrons involved in the thermal process is proportional to electronic temperature $n_e \propto n_a T_e / T_g$ as long as $T_e < T_g$. A more refined estimation could have been made by adding the continuity equation for carrier density [28]. We adopt an intermediate point of view which consists in considering that the number of electrons varies within the bandgap in accordance with the idea proposed by Daraszewicz *et al* [28]. Following their idea, we note the difference between our concept (energy diffusion dominated by the temperature gradient) and their idea (energy diffusion dominated by carrier diffusion). Finally, all the refinements proposed to Awazu's work [19] lead to important results, as is shown below.

2.4. Electron-phonon coupling constant g

The electron–phonon coupling constant g has been studied in supraconductors [29, 30] and the formulation of g has been successfully extended to other types of materials (metals [14, 15, 31, 32], semiconductors and insulators [18, 33]). We use the values reported in the latter references. The values of g and K_e are consistent with the ones used by Toulemonde *et al* [18, 33] since the mean free path λ ($\lambda^2 = K_e/g$) remains unchanged between this paper and those references. When we compare our results with the previous studies, we choose $g_{crystalline \, SiO_2} = 1.25 \times 10^{13} \, \text{W cm}^{-3} \, \text{K}^{-1}$ (see section 3.1), whereas for the following sections (from section 3.2) we use $g_{amorphous \, SiO_2} = 3.2 \times 10^{13} \, \text{W cm}^{-3} \, \text{K}^{-1}$.

Considering all the remarks above, we can now report in table 1 all the thermodynamical parameters used for the calculations.

3. Results and discussion

3.1. Comparison with previous calculations: cylindrical particles

In this section, we make the link between this study and the work previously published by Awazu *et al* [19]. In order to confirm the accuracy of the present 3D version of the thermal spike code, we have performed simulations first in bulk gold and silica, and then in the case of gold cylindrical nanoparticles with 10 and 20 nm diameter embedded in silica with thermodynamic parameters used in [19]. The results are perfectly consistent with [19] regarding the maximal temperatures as well as the heating and cooling times. We plot both electronic and atomic temperature evolutions as a function of time (abscissa) and radial distance to the ion path (ordinate) for a gold particle 20 nm in diameter (figure 5). Similarly to the simulation done in [19], the gold nanoparticles do not melt. This is due to the fact that the electronic heat distributed over the particle spreads out and is transferred to silica atoms within 10^{-12} s, while this time is too short for the gold lattice to heat up due to the low g-factor.

However, the elongation of such nanoparticles [19], and even larger ones (40 nm [34]), was observed experimentally.

We show the very different behaviour (see figure 6) if we use the $K_e(T_e)_{SiO_2}$ value (figure 4) as previously discussed (see section 2.3). Up to $t \approx 2 \times 10^{-14}$ s, the electronic temperature for both cases is similar, but for greater times, (figure 5(a)), the temperature increase spreads out of the nanoparticle, while hot electrons are confined within the particle (figure 6(a)) so that T_e remains higher than 3000 K for times as long as 3×10^{-12} s inside the particle as well as in the thin SiO_2/particle interface layer. Due to a high g-factor, the electronic heat is efficiently transferred to the silica atoms so that the SiO_2 lattice temperature increases in this interface layer. Finally, due to lattice thermal diffusion, the lattice temperature of the metallic nanoparticle rises. The heating of nanoparticle atoms occurs
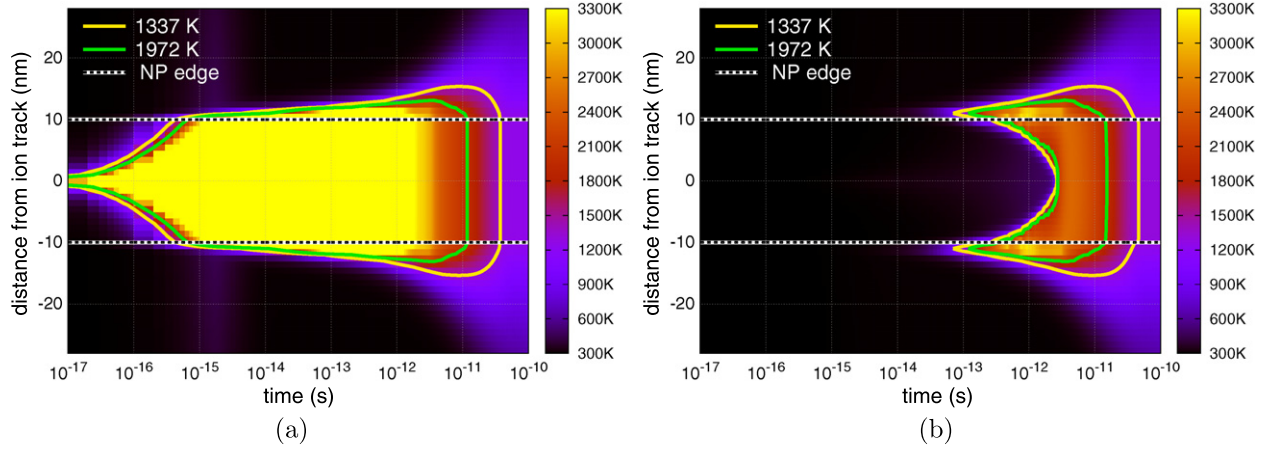
Figure 6. Cylindrical gold nanoparticle (diameter: 20 nm). Evolution of the electronic and atomic temperatures $T_e(r, t)$ and $T_a(r, t)$ in kelvin as a function of radial distance r from the ion path and time t. The thermodynamic parameters and the thermal conductivities $K_{e_{SiO_2}}$ and $K_{a_{Au}}$ are those of this work.
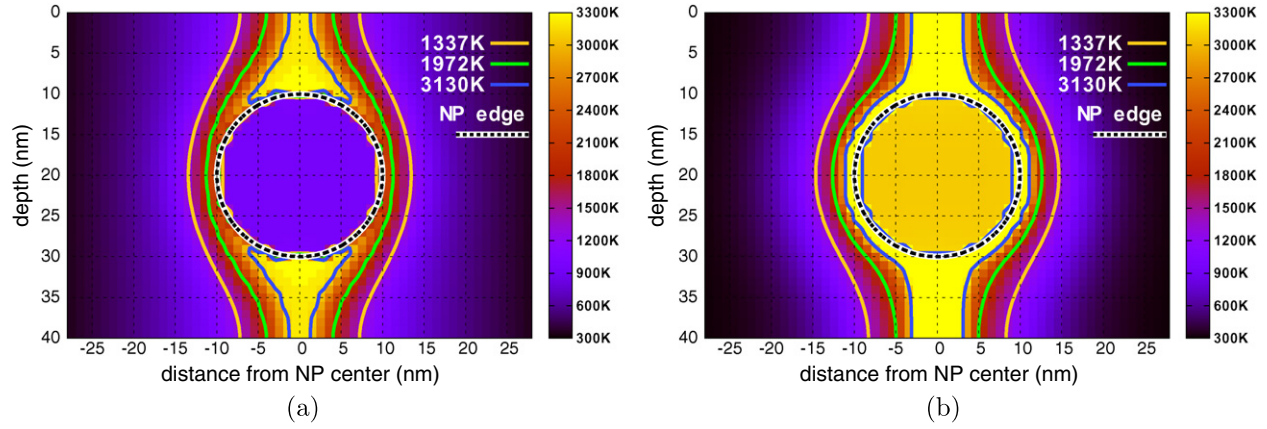

Figure 7. Maximum lattice temperature reached around a gold nanoparticle (diameter = 20 nm). Physical parameters: (*a*) Awazu *et al* [19], (*b*) this paper. Contour lines correspond to Au melting temperature (1337 K), SiO$_2$ melting temperature (1972 K), Au vaporizing temperature (3130 K). The dotted blue line is the boundary of the metallic particle.

from the outer layers towards the core until complete particle melting (see figure 6(*b*)). This process takes time from 10^{-13} to 3×10^{-12} s, then both electronic and lattice subsystems are in equilibrium and cool down until the particle is solidified at about 5×10^{-11} s.

3.2. Spherical gold nanoparticles

Actually, the simulations from the previous section, both ours and those described in [19], were performed in the 2D xy-plane perpendicular to the swift heavy ion track which avoids investigations as a function of depth (z-coordinate). Now, we deal with spherical particles embedded in a matrix so that the third coordinate is required since the incoming ion first penetrates the matrix and then the particle. We again compare the simulations resulting from the parameter set used by Awazu *et al* [19] and the present one for two particle sizes.

3.2.1. Gold nanoparticle 20 nm in diameter: role of the thermal conductivity at the SiO$_2$ interface.
The maximum lattice temperature reached in a spherical gold particle (20 nm

in diameter) is shown in figure 7. One can see that in the case of Awazu's parameters (left hand side), only silica regions close to the ion path or to the particle surface are hot, since they are provided with a high electronic temperature at the early stage of the thermal process. The outside area and the inner zone of the particle remain relatively cold. In contrast, if we account for the thermal conductivity described in section 2.3) (right-hand side of figure 7), we observe a very hot track in silica, a completely molten nanoparticle with vaporized surface layer. These results are similar to those of the previous section, but the extra heat comes to the particle polar regions from neigbouring silica.

3.2.2. Gold nanoparticle 40 nm in diameter: influence of the gold lattice thermal conductivity.
Another peculiarity can be found for larger particles which are not completely molten (figure 8). Concerning the proper choice of lattice thermal conductivity in a metal, as we mentioned above, the measured values are not adequate since they mostly represent the electronic part of thermal conductivity. The molten phase
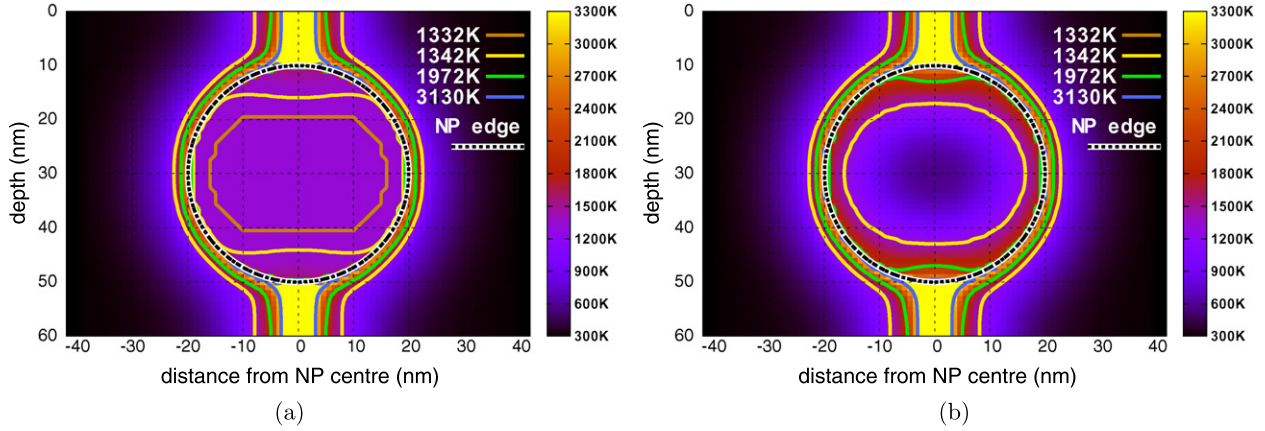
(a)   (b)

Figure 8. Maximum lattice temperature reached in a gold particle ($d = 40$ nm), using different thermal conductivities (K_a): (*a*) K_a taken from Awazu [19], (*b*) our proposal (see section 2.2). Contour lines correspond to the melting points: 1332K—T_{m-}(gold), 1342 K—T_{m+} (gold), 1972 K—T_m (SiO$_2$). 3130 K is the vaporizing temperature of gold.
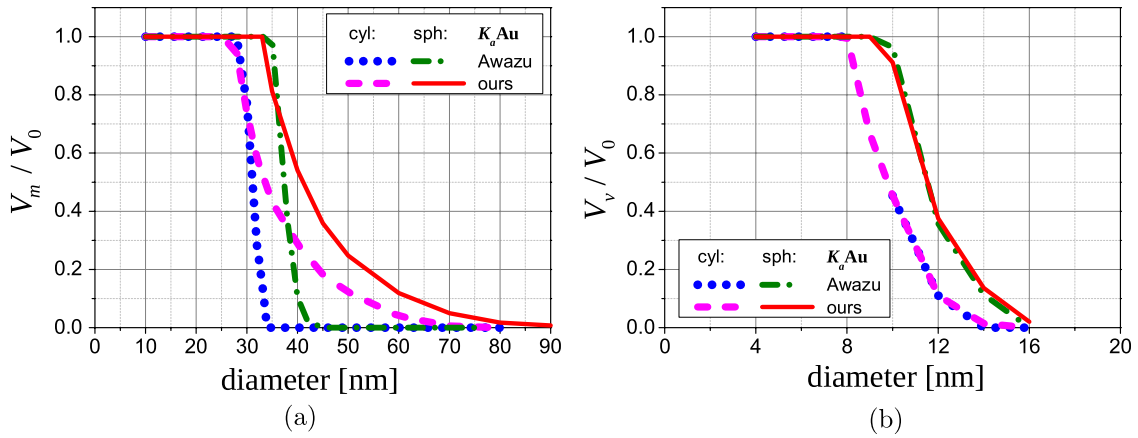

(a)   (b)

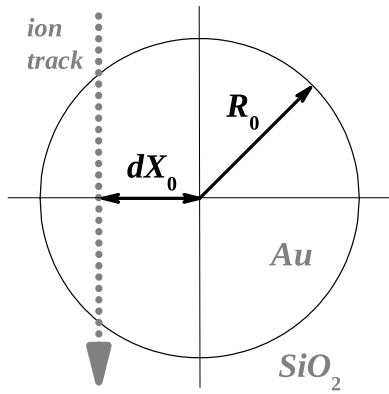**Figure 9.** Molten (*a*) and vaporized (*b*) fraction versus particle diameter.

Figure 10. Off-axis impact layout.

on the plots is presented with double curves, at $T_m \pm \Delta T$ (1332 and 1342 K). It can be seen that, with measured values of K_a (figure 8(*a*)), an extended region reaches melting point (T_{m-} contour), though only a small fraction has surpassed the melting latent heat (T_{m+} contour). With the correct K_a value (figure 8(*b*)), both contours coincide and the volume of complete melting is much larger, while the core temperature remains lower than in figure 8(*a*).

3.3. Melting and vaporization of nanoparticles with different sizes

The volumic molten and vaporized fraction versus initial particle diameter is shown in figure 9 for both spherical and cylindrical particles with two kinds of lattice thermal conductivity of gold and interfacial electronic thermal conductivity. As we showed above, if we do not account for the interfacial region, melting is not observed even for 20 nm particles.

The relative molten and vaporized volumes are systematically higher for 3D-spherical particles in comparison with cylindrical ones. We can suppose that the energy deposited in the nanoparticle by the incident ion is then confined and evenly distributed over the whole volume of the particle. The value $\varepsilon = (cS_e l / V N_a)$ gives the energy density per atom received from a swift heavy ion. Here l is the ion path inside the particle, V and N_a are particle volume and atomic concentration. For a cylinder with a radius R, $\varepsilon_{cyl} = (S_e/\pi R^2)$, while for a sphere $\varepsilon_{sph} = \frac{3}{2}\frac{S_e}{\pi R^2}$ (in the case of central ion hit). Naturally, the molten and vaporized volumic fractions are higher for the spherical particle than for the cylindrical one of the same diameter. The heat exchange between metal and silica around the ion spot also plays an important role.
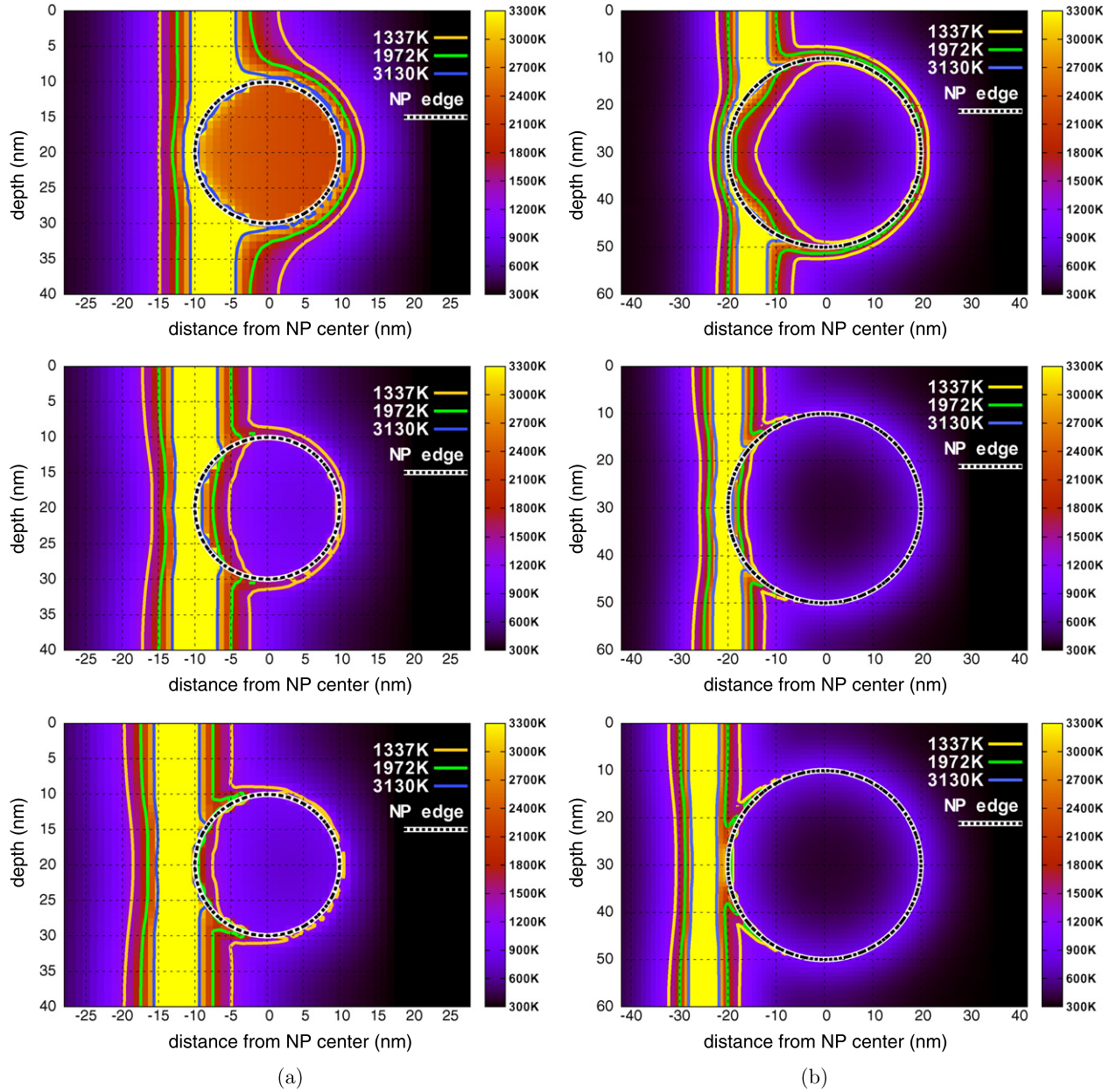
Figure 11. Maximum lattice temperature as a function of the ion path distance $dX_0 = R_0 \cdot \Delta$ from the centre of a gold nanoparticle of radius R_0. Particle diameter: (*a*) 20 nm; (*b*) 40 nm; from top to bottom: $\Delta = \frac{3}{4}, 1, \frac{5}{4}$.

Complete melting is observed for particle diameters up to 30 nm. For larger particles, if the energy deposited by the incident ion is not high enough to melt the whole particle, then, with experimental gold lattice thermal conductivity, the molten fraction quickly drops to zero, while using K_a derived from the equation in section section 2.2, the molten fraction slowly decreases, remaining non-zero up to 70–80 nm.

As for vaporization, there is no difference if we account for the thermal conductivity from [19] or from this work, since, above the melting point both parameters are the same. The particles with a diameter between 10 and 15 nm are partially vaporized, while below 10 nm, complete vaporization is observed. Such small particles undergo dissolution and may precipitate into larger particles.

3.4. Full 3D: effect of off-axis impact

3.4.1. Temperature distribution. Using the 3D capabilities to treat any problem without any symmetry, we focus on the effect of an ion off-axis impact (figure 10). We performed simulations within diameter range from 10 to 80 nm at different offset values: $\Delta = dX_0/R_0 = n/4$, n varied from 1 to 6.

The most interesting was to see what happens when the ion hits the particle close to its edge. The corresponding plots are shown in figure 11 for 20 and 40 nm nanoparticles and $\Delta = \frac{3}{4}, 1, \frac{5}{4}$ (the central impacts for them are shown in figures 7(*b*) and 8(*b*)). Two remarks arise from the results: (i) in non-central impacts, the melting of the particle still starts from the surface, (ii) the particle lattice temperature
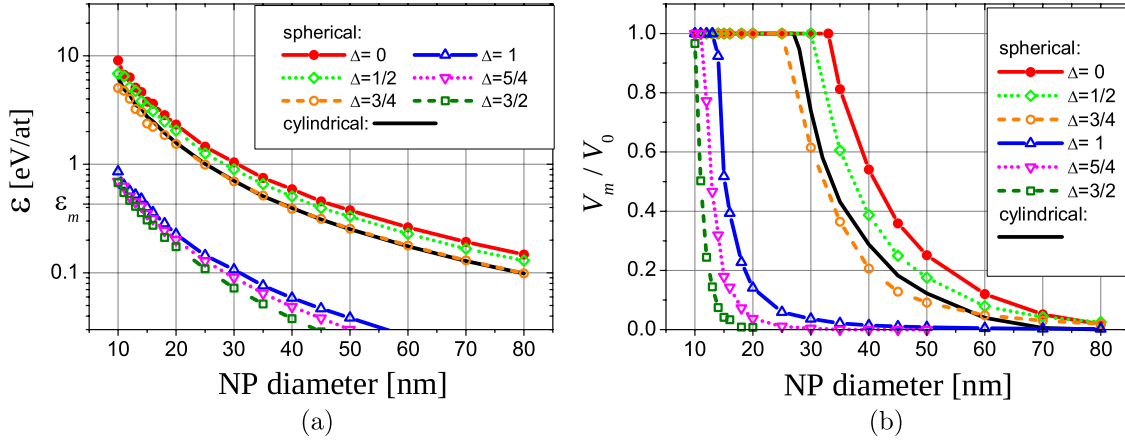
Figure 12. Deposited energy density (*a*) and molten volume fraction (*b*) versus the gold nanoparticle diameter for different values of the offset Δ.

significantly increases only if the ion path effectively intercepts the particle (i.e. $\Delta \leqslant 1$).

3.4.2. Energy density and molten volume. We studied the influence of the ion impact parameter on the behaviour of cylindrical and spherical nanoparticles. The deposited energy density ε (figure 12(*a*)) and the molten volume fraction V_m/V_0 (figure 12(*b*)) are plotted as a function of the particle diameter for different ion path offsets Δ. First, there is a difference depending on whether the incident ion enters the particle ($\Delta < 1$) or not ($\Delta \geqslant 1$). In the latter case, only a small amount of energy is deposited due to secondary δ-electrons penetrating inside the particle. However, this is enough to melt nanoparticles smaller than $\sim$20nm in radius.

If $\Delta < 1$, ε is all the larger as Δ is low, which is natural for spherical particles. A similar correlation is observed concerning the molten volume fraction. The corresponding curve for cylindrical particles does not depend on the value of the impact offset Δ provided that $0 < \Delta < 1$ (i.e. when the ion strikes the particle).

Then, comparing the deposited energy density for spherical $\varepsilon_{sph} = \frac{3}{2} \frac{S_e}{\pi R^2} \sqrt{1 - \Delta^2}$ and cylindrical particles $\varepsilon_{cyl} = \frac{S_e}{\pi R^2}$, one can see that for $\Delta = \sqrt{5}/3 \approx 3/4$, $\varepsilon_{sph} = \varepsilon_{cyl}$. The $\varepsilon(d)$ curves really coincide for this latter case (figure 12(*a*)), but due to electronic heat leakage from the particle to the surrounding silica within the ion spot area, up to 60 nm the molten volume fraction for spherical particles is smaller than for cylindrical ones. However, starting from 60 nm diameter, all spherical particles intercepted by ion ($\Delta < 1$) demonstrate stable molten fraction above $\sim$2%, because heated particle–SiO$_2$ interface keeps the temperature high enough to melt the metal.

We estimate the energy density needed to melt the whole particle as $\varepsilon_m = (\int_{T_0}^{T_m} C_a \, dT_a + \rho_S Q_m)/N_a$. For gold $\varepsilon_m = 0.43 \, \text{eV atom}^{-1}$. However, comparing figure 12(*a*) and (*b*), one can see that the energy necessary for complete NP melting is approximately twice as large as ε_m (from 0.8 to 1 eV atom^{-1}). This is due to heat leakage outside the particle and can be taken into account for the estimation with other particles and ions.

4. Conclusion

We presented the first real 3D implementation of thermal spike model devoted to the simulation of swift heavy ion interaction with any kind of composite structures. Thermal behaviour of metallic nanoparticles embedded in amorphous matrix has been studied. To obtain results consistent with irradiation induced particle elongation, the thermodynamical parameters should follow the characteristics described hereafter. The target electrons are considered as a quasi-free electron gas with classical specific heat and thermal diffusivity, whereas the target lattice is characterized with thermal coefficients based on statistical physics. Experimentally measured thermodynamical parameters for metals cannot be used here, as they are a combination of properties of the electronic and lattice subsystems, and therefore neither subsystem is properly described. Using the 3D approach, we can make the distinction between cylindrical and spherical particles and show the influence of energy exchange on the metal/silica interface around the ion spot. Using the metallic (nanoparticle) and dielectric (matrix) thermal properties, it is shown that the heating of nanoparticle starts from the outer layer towards the core. This provides conditions for partial melting when there is not enough energy to melt the whole nanoparticle. We demonstrate the influence of the impact parameter (i.e. radial distance between the ion path and the spherical nanoparticle centre): (i) a large particle (diameter 60 nm) partially melts in the case of an ion path tangent to the particle surface due to large particle/matrix interfacial area; (ii) a small particle ($\leqslant$60 nm) can be molten even if the ion does not directly strike it. This is due to heat transfer from molten silica track of about 10 nm in diameter.

The thermal effect of the ion is all the higher as the impact is close to the particle centre because of a larger amount of deposited energy and lower energy leakage outside the particle. Thus, elongation could preferably occur from the central axis of the particle. This effect will increase in the case of an ion striking an elongated particle along the elongation axis since the ion path inside the particle will be longer.

The simulations proposed in this work describe the melting of metallic nanoparticles irradiated with swift heavy

ions and, and, thus, provide a background for understanding of ion shaping effect.

Acknowledgments

References

[1] D'Orleans C, Stoquert J, Estournes C, Cerruti C, Grob J, Guille J, Haas F, Muller D and Richard-Plouet M 2003 *Phys. Rev. B* **67** 220101

[2] Singhal R, Agarwal D C, Mishra Y K, Singh F, Pivin J C, Chandra R and Avasthi D K 2009 *J. Phys. D: Appl. Phys.* **42** 155103

[3] Mishra Y K, Avasthi D K, Kulriya P K, Singh F, Kabiraj D, Tripathi A, Pivin J C, Bayer I S and Biswas A 2007 *Appl. Phys. Lett.* **90** 073110

[4] Kuiri P K, Joseph B, Ghatak J, Lenka H P and Sahu G 2010 *Adv. Sci. Lett.* **3** 404

[5] Kumar K, Mukesh A, Ganesan P G, Singh V N, Mehta B R and Singh J P 2008 *Nanotechnology* **19** 175606

[6] Mishra Y K, Singh F, Avasthi D K, Pivin J C, Malinovska D and Pippel E 2007 *Appl. Phys. Lett.* **91–94** 063103

[7] Singh F, Mohapatra S, Stolquert J P, Avasthi D K and Pivin J C 2009 *7th Triennial Int. Symp. on Swift Heavy Ions in Matter (Lyon, France, 02–05 June, 2008) Nucl. Instrum. Methods* B **267** 936

[8] Silva-Pereyra H G, Arenas-Alatorre J, Rodriguez-Fernandez L, Crespo-Sosa A, Cheang-Wong J C, Reyes-Esqueda J A and Oliver A 2010 *J. Nanopart. Res.* **12** 1787

[9] Rizza G, Cheverry H, Gacoin T, Lamasson A and Henry S 2007 *J. Appl. Phys.* **101** 014321

[10] Rizza G, Dawi E A, Vredenberg A M and Monnet I 2009 *Appl. Phys. Lett.* **95** 043105

[11] Dawi E A, Rizza G, Mink M P, Vredenberg A M and Habraken F H P M 2009 *J. Appl. Phys.* **105** 074305

[12] Ridgway M C *et al* 2011 *Phys. Rev. Lett.* **106** 095505

[13] Toulemonde M, Dufour C and Paumier E 1992 *Phys. Rev. B* **46** 14362

[14] Dufour C, Audouard A, Beuneu F, Dural J, Girard J, Hairie A, Levalois M, Paumier E and Toulemonde M 1993 *J. Phys.: Condens. Matter.* **5** 4573–84

[15] Wang Z, Dufour C, Paumier E and Toulemonde M 1994 *J. Phys.: Condens. Mat.* **6** 6733

[16] Wang Z, Dufour C, Paumier E and Toulemonde M 1995 *J. Phys.: Condens. Mat.* **7** 2525

[17] Toulemonde M, Constantini J, Dufour C, Meftah A, Paumier E and Studer F 1996 *8th Int. Conf. on Radiation Effects in Insulators (REI-8)—Beam Interactions with Materials and Atoms (Catania, Italy, 11–15 September, 1995) Nucl. Instrum. Methods* B **116** 37

[18] Toulemonde M, Dufour C, Meftah A and Paumier E 2000 *10th Int. Conf. on Radioation Effects in Insulators (REI-10) (Jena, Germany, 18–23 July, 1999) Nucl. Instrum. Methods* B **166** 903

[19] Awazu K, Wang X, Fujimaki M, Tominaga J, Aiba H, Ohki Y and Komatsubara T 2008 *Phys. Rev. B* **78** 054102

[20] Ziegler J F, Ziegler M D and Biersack J P 2010 *19th Int. Conf. on Ion Beam Analysis (Cambridge, England, 07–11 September, 2009) Nucl. Instrum. Methods* B **268** 1818

[21] Waligorski M, Hamm R and Katz R 1986 *Nucl. Tracks Radiat. Meas.* **11** 309

[22] Meftah A, Brisard F, Constantini J M, Dooryhee E, Hage-Ali M, Hervieu M, P S J, Studer F and Toulemonde M 1994 *Phys. Rev. B* **49** 12457

[23] Lide D R 2006 *CRC Handbook of Chemistry and Physics, A Ready- Reference Book of Chemical and Physical Data* (Boca Raton, FL: CRC Press)

[24] Perry R H and Green D W 1984 *Perry's Chemical Engineers' Handbook* (New York: McGraw-Hill)

[25] Touloukian Y S, Powell R W and Ho C Y 1970 *Thermophysical Properties of Matter* (New York: IFI/Plenum)

[26] Ashcroft N W and Mermin N D 1976 *Solid State Physics* (New York: Holt Reinhart and Winston)

[27] Martynenko Y V and Yavlinskii Y N 1983 *Sov. Phys.—Dokl.* **28** 391

[28] Daraszewicz S L and Duffy D M 2011 *Nucl. Instrum. Methods* B **269** 1646

[29] Kaganov M I, Lifshitz I M and Tanatarov L V 1957 *Sov. Phys.—JETP-USSR* **4** 173

[30] Allen P 1987 *Phys. Rev. Lett.* **59** 1460

[31] Dufour C, Wang Z, Levalois M, Marie P, Paumier E, Pawlak F and Toulemonde M 1996 *3rd Int. Conf. on Swift Heavy Ions in Matter (SHIM 95) (Caen, France, 15–19 May, 1995) Nucl. Instrum. Methods* B **107** 218

[32] Dufour C, Paumier E and Toulemonde M 1997 *Proc. E-MRS '96 Spring Meeting Symposium K on Nanometric Phenomena Induced by Laser Ion and Cluster Beams (Strasbourg, France, 04–07 June, 1996) Nucl. Instrum. Methods* B **122** 445

[33] Toulemonde M, Weber W J, Li G, Shutthanandan V, Kluth P, Yang T, Wang Y and Zhang Y 2011 *Phys. Rev. B* **83** 054106

[34] Awazu K, Wang X, Komatsubara T, Watanabe J, Matsumoto Y, Warisaws S and Ishihara S 2009 *Nanotechnology* **20** 325303